Earth Planets Space, **61**, 1243–1254, 2009

Simulation of mode conversion from UHR-mode wave to LO-mode wave in an inhomogeneous plasma with different wave normal angles

Mohammad Javad Kalaee, Takayuki Ono, Yuto Katoh, Masahide Iizima*, and Yukitoshi Nishimura†

Department of Geophysics, Graduate School of Science, Tohoku University, Japan

(Received September 21, 2008; Revised June 29, 2009; Accepted July 24, 2009; Online published December 21, 2009)

We have investigated a linear mode conversion process among UHR-mode, Z-mode, and LO-mode waves by a computer simulation solving Maxwell's equations and the motion of a cold electron fluid. The characteristics of the wave coupling process occurring in the cold magnetized plasma were examined in detail for the case of an inhomogeneity of plasma density lying perpendicular to the ambient magnetic field. The dependence of the conversion efficiency on the incident wave normal angle, wave frequency, background plasma frequency, and steepness of density gradient was studied. The results show that an efficient mode conversion occurred in the conversion process from Z-mode to LO-mode waves rather than from the coupling between UHR-mode to LO-mode waves. They also show that the highest conversion efficiency was obtained under the specific condition of the wave normal angle for the incident waves. In the specific case of such critical wave normal angles, we found that perpendicular components of refractive indexes became zero at the site of mode conversion, which is consistent with previously published results. We also show that the range of the critical normal angle varied depending on both the plasma frequency and the wave frequency. The simulation results also reveal that, when the steepness of the density gradient was taken into consideration, efficient mode conversion could be expected even in the case of the mismatch of the refractive indexes preventing the close coupling of plasma waves.

Key words: Mode conversion, numerical simulation, LO-mode, wave generation process.

1. Introduction

A large variety of plasma waves exist in space plasmas, depending on the conditions of the medium. The refractive index is determined by the characteristics of waves, such as the wave frequency and the wave normal angle, and by plasma parameters, such as the number density of the plasma and the background magnetic field strength. In an inhomogeneous plasma where these parameters vary as a function of position, the local refractive index is a function of position (Stix, 1992). The mode conversion, identified as a change in the propagation modes of plasma waves, is one of the generation mechanisms of radio emissions occurring in an inhomogeneous plasma. MjΦlhus (1983, 1990) discussed the linear mode conversion of an ordinary polarized electromagnetic wave in a magnetized plasma with a density gradient parallel to the magnetic field and developed an expression for the conversion coefficient as a function of the incident wave normal angle. The magnetic field leads to a narrowing of the range of angles of incidence, leading to linear conversion when compared with the case of the unmagnetized field.

The mode conversion of upper-hybrid-resonance (UHR) mode waves ($\omega_p < \omega \leq \omega_{uh}$) to Z-mode ($\omega_z < \omega \leq \omega_p$) and LO-mode waves has been investigated for the purpose of understanding the origin of planetary radio emissions, where ω is the wave frequency, ω_p is the electron plasma frequency, ω_{uh} is the upper hybrid resonance frequency, and ω_z is the cutoff frequency of Z-mode. The mode conversion theory proposed by Oya (1971) has been applied for the generation process of Jovian decametric radiation (Oya, 1974) and auroral kilometric radiation (AKR) (Benson, 1975). Oya (1974) assumed a sharp boundary in the vicinity of the position where $\omega = \omega_p$. He showed that conversion rates of 1–50% are obtained when a wave normal direction of an incident wave is nearly parallel to the boundary normal direction while the Jovian magnetic field vector is close to the boundary normal direction within an angle range of 10–15°. He also showed that the conversion rate becomes lower and lower when the angle between the boundary normal direction and the magnetic field vector become larger and larger. Even though his result is limited up to 75°, it can be suggested that the conversion rate becomes very low for the perpendicular case.

The mode conversion mechanism consists of three processes. In the first process, field-aligned precipitating beams and/or anisotropies of velocity distribution of energetic electrons create electrostatic electron cyclotron harmonic waves. These electrostatic waves propagate toward lower plasma density regions until these waves encounter the electrostatic resonance frequency, as has been experimentally identified by Warren and Hagg (1968). In the second process, the electrostatic electron cyclotron harmonic waves are converted to UHR mode waves, being reflecting

*Now at Shukutoku University, Japan.

†Now at Solar-Terrestrial Environment Laboratory, Nagoya University, Japan.

Copyright © The Society of Geomagnetism and Earth, Planetary and Space Sciences (SGEPSS); The Seismological Society of Japan; The Volcanological Society of Japan; The Geodetic Society of Japan; The Japanese Society for Planetary Sciences; TERRAPUB.

back toward higher plasma density. These waves are further converted to the Z-mode radio waves toward the high-density region. In the third process, the Z-mode waves propagate into the plasma frequency layer of $\omega = \omega_{pe}$, where these waves have a chance to convert into ordinary (LO-mode) waves. There are a number of variations of the conversion mechanisms to explain the radiation of LO-mode waves from the planetary plasma. A typical example is non-thermal continuum radiation, which is one of the common radio emissions in planetary magnetospheres. Jones (1977) proposed the conversion process of continuum radiation in which Z-mode waves are directly generated by energetic electrons and then converted to the LO-mode wave in the region close to the plasmapause. The fundamental characteristics of observed continuum radiation have been explained by the proposed mechanism (Jones, 1980, 1987). Observations and theories have been summarized by Hashimoto *et al*. (2006).

The linear mode conversion process has been mainly studied by assuming the Wentzel-Kramers-Brillouin (WKB) approximation in which the spatial scale of an inhomogeneity is large enough relative to the wave length of incident waves. However, observational results show that the WKB approximation would often be violated in the magnetosphere during disturbed periods. Also, a difficulty in theoretical treatment arises when the waves encounter a resonance layer, as has been discussed by Takano *et al*. (2005). A numerical experiment can be a highly useful tool for a guiding theory in discussions of mode conversion processes under such an environment. Using a full-particle code, Ueda *et al*. (1998) studied a conversion process from LO-mode waves to UHR-mode waves in association with ionospheric plasma heating. An finite-difference time-domain (FDTD) simulation of the wave coupling process was performed by Kim *et al*. (2005), although their simulation parameters were different from the magnetospheric condition. However, the mode conversion process in the magnetosphere has not yet been studied, and a self-consistent simulation that is free from the WKB approximation has not been used in previous studies. In the study reported here, we discuss the properties of mode conversion processes by performing numerical experiments with different wave normal angles and different incident wave frequencies under the same plasma conditions, such as plasma frequency and steepness of the density gradient. Based on the simulation results, we discuss the parameter dependence of conversion efficiency on the direction of the propagation vector. The dependence of the conversion efficiency on the background plasma frequency and steepness of density gradient is also studied. We describe the simulation model used in our study in Section 2. Simulation results and characteristics of mode conversion process are discussed in Section 3. Section 4 provides a summary.

2. Simulation Model

We have studied the wave coupling process among UHR-mode, Z-mode, and LO-mode waves using a two-dimensional (2D)-electron fluid model that was also used by Katoh (2003) and Katoh and Iizima (2006). We assume

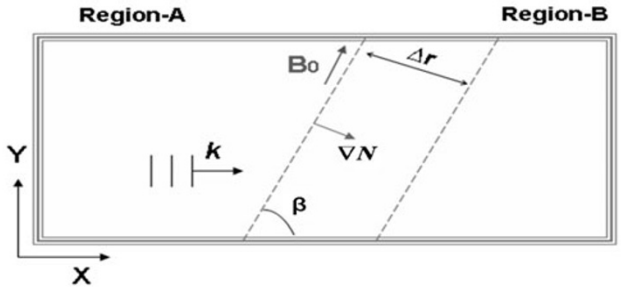

Fig. 1. Schematic of illustration of the simulation system. We assume homogenous regions with plasma frequencies of ω_{pA} (Region-A) and ω_{pB} (Region-B) smoothly connected by an inhomogeneous region where the density gradient ∇N is assumed with the spatial scale of $\Delta \boldsymbol{r}$.

that the simulation system is immersed in a plasma medium of a cold plasma fluid. The basic equations are given as follows;

$$\frac{\partial V}{\partial t} = -(V \cdot \nabla)V + \frac{q}{Nm}(E + V \times B) \tag{1}$$

$$\frac{\partial N}{\partial t} = -\nabla \cdot (NV) \tag{2}$$

$$\frac{\partial B}{\partial t} = -\nabla \times E \tag{3}$$

$$\frac{\partial E}{\partial t} = \frac{1}{\varepsilon_0 \mu_0}\nabla \times B - \frac{1}{\varepsilon_0} J \tag{4}$$

where E, B, J, V, and N represent the electric field, magnetic field, current density, velocity, and number density of the electron fluid, respectively. The equation of motion and continuity equations coupled with Maxwell's equations are solved using the two-step Lax-Wendroff scheme. Each physical value is normalized to a dimensionless quantity, with time normalized by electron cyclotron frequency (ω_c), and velocity and length normalized by the speed of light c and c/ω_c, respectively. We assume grid spacing ΔX and ΔY as $1 \times 10^{-2} c/\omega_c$ and time step Δt as $7.5 \times 10^{-3} \omega_c^{-1}$. The numbers of grids are assumed to be from 5000 up to 7500 in the X-direction and from 4000 up to 5000 in the Y-direction, while each set of values is determined by the spatial scale required to describe the angle θ in the simulation system.

Figure 1 schematically indicates the 2D simulation box used in our study. The external magnetic field $\boldsymbol{B}_0$ is assumed to be in the X-Y plane, with an angle β against the X-axis. The simulation box consists of three regions: homogeneous regions with plasma frequencies of ω_{pA} (Region-A) and ω_{pB} (Region-B), respectively, smoothly connected by an inhomogeneous region. The width Δr of the inhomogeneous region parallel to the density gradient is about $5\lambda_{UHR}$, where λ_{UHR} is the wave length of incident UHR waves. The density gradient is directed perpendicular to $\boldsymbol{B}_0$ as a function of the X and Y coordinates. We can estimate a scale length L of the density gradient using

$$L^{-1} = \left\langle \frac{1}{N}\frac{dN}{dr} \right\rangle = \frac{1}{N}\frac{\Delta N}{\Delta r} \tag{5}$$

to obtain a value of $L^{-1} \approx 0.108\lambda^{-1}$. We changed the width of the inhomogeneous region in each simulation run

so as to satisfy the condition in which the spatial scale of the density gradient corresponds to five wavelengths of the incident waves.

We generate plasma waves by oscillating the E_x and E_z components in the wave generation region, while the wave vector k of the generated waves is introduced to be aligned along the x-axis that describes the direction, making an oblique propagating to the external magnetic field. The initial wave form is given by

$$E_x(x, y, t) = A_x(x) \cdot A_y(y) \cdot A_t(t) \cdot E_{0x}(x, t), \quad (6)$$

$$E_z(x, y, t) = C_0 \cdot A_x(x) \cdot A_y(y) \cdot A_t(t) \cdot E_{0z}(x, t). \quad (7)$$

Here

$$E_{0x}(x, t) = E_{W0}\, e^{i(k_0 x - \omega_0 t)}, \quad (8)$$

$$E_{0z}(x, t) = E_{W0}\, e^{i(k_0 x - \omega_0 t + \pi/2)}, \quad (9)$$

$$A_x(x) = \begin{cases} \exp\left\{-\left(3\dfrac{x - X_0}{\delta X}\right)^2\right\} \\ \qquad : X_0 - \delta X < x < X_0 + \delta X \\ 0 \qquad : \text{else} \end{cases} \quad (10)$$

$$A_y(y) = \begin{cases} \exp\left\{-\left(3\dfrac{y - Y_0}{\delta Y}\right)^2\right\} \\ \qquad : Y_0 - \delta Y < y < Y_0 + \delta Y \\ 0 \\ \qquad : \text{else} \end{cases} \quad (11)$$

$$A_t(t) = \begin{cases} \dfrac{t}{T_s} \qquad : t < T_s \\ 1. \qquad : T_s < t < 6T_s \\ 1 - \dfrac{(t - 6T_s)}{T_s} : 6T_s < t < 7T_s \end{cases} \quad (12)$$

where C_0 is the ratio between E_x and E_z of incident plasma waves determined from cold plasma dispersion relation, k_0 and ω_0 are the wavenumber and frequency of incident waves, respectively, E_{W0} is the initial wave amplitude, $T_s = 5\omega_e^{-1}$, $\delta X = 4c\omega_e^{-1}$, $\delta Y = 4c\omega_e^{-1}$, and (X_0, Y_0) is the center point of the generation region. To avoid any effects due to reflected waves from the boundary of the simulation box, we set damping regions at the edges of the simulation system to suppress the reflection of outgoing waves.

Here, we discuss two cases of the mode conversion process. In the first case, we consider the "single" mode conversion process from UHR-mode wave to Z-mode and LO-mode waves. In the second case, we consider the "double" mode conversion process not only from UHR-mode wave to Z-mode and LO-mode waves but also from Z-mode to LO-mode and UHR-mode waves.

3. Results and Discussion

3.1 Case 1: single-mode conversion

In the first step, we consider the single-mode conversion process form UHR-mode wave to Z-mode and LO-mode waves. We assume ω_{pB} so that the incident wave frequency is below ω_{pB} but above the cutoff frequency of the Z-mode in the Region-B. Under this condition, the incident waves converted to the Z-mode can transmit into the Region-B without reflection. Therefore, the condition of the single-mode conversion process is achieved in the simulation system. We performed six runs with different wave normal angles under the same plasma conditions, as given in Table 1. We assume $\omega_{pA}/\omega_c = 2.0$ and $\omega_{pB}/\omega_c = 2.0317$. In the simulation results, we observed the generation of LO-mode wave through the mode conversion process.

In order to examine the coupling properties between UHR-mode and LO-mode waves, we performed Fast Fourier transform (FFT) analysis on both the wave electric field and magnetic field to obtain the spatial distributions of frequency and wave number spectra. In each simulation run, we confirmed that the polarization of the incident wave is according to the UHR wave. We estimated the wave normal angle of the converted LO-mode wave by analyzing its polarization. In Runs 1-A to 1-E, the wave normal vectors of the converted LO-mode wave are almost parallel to the external magnetic field.

In Fig. 2, we show the variation in the wave number $\boldsymbol{k}$ of plasma waves with the wave frequency of $\omega = 2.03\omega_c$, with the specific propagation angles as a function of ω_p/ω_c, where ω_p is the local plasma frequency. The point A in the diagram indicates the position of the incident wave generated in simulation box. In the case that the incident UHR waves propagate into the region where the local plasma fre-

Table 1. Summary of simulation results and parameters used in case 1 (with $\omega_{pA} = 2\omega_c$ and $\omega_{pB} = 2.0317\omega_c$) consist of wave normal angle, incident wave frequency, wave length, ratio of electric field components and efficiency. By performing FFT analyses, we obtained three components of wave amplitudes, wavenumber and frequency spectra of both incident and converted waves. By analyzing their polarization, we estimated the wave normal angles. For the reference we also show the polarization of each mode estimated by the dispersion relation of cold plasma.

	Wave normal Angle(θ)	Frequency of wave ω/ω_c	wave length $\lambda[c\Omega^{-1}]$	wave mode	(FFT analyses) E_x/E_z	E_y/E_z	(Dispersion relation) E_x/E_z	E_y/E_z	E_Z	Efficiency
Run 1-A	30	2.03	0.363	UHR	7.08	0.199	7.07	0.198	2.5e-5	4.0e-12
	≈10		0.907	LO	2.35	0.35	2.4	0.33	2.0e-10	
Run 1-B	45	2.03	0.431	UHR	3.64	0.0	3.64	0.083	1.5e-5	1.6e-4
	≈10		0.907	LO	2.2	0.91	2.23	0.93	8.0e-8	
Run 1-C	58	2.03	0.451	UHR	2.78	0.042	2.78	0.043	4.0e-5	8.6e-4
	≈8		0.879	LO	1.73	0.95	1.73	0.98	4.0e-7	
Run 1-D	75	2.03	0.461	UHR	2.3	0.015	2.34	0.016	5.0e-5	1.0e-4
	≈9		0.893	LO	1.4	1.66	1.41	1.68	3.0e-8	
Run 1-E	85	2.03	0.463	UHR	2.2	0.007	2.25	0.005	5.0e-5	5.4e-14
	≈10		0.907	LO	1.0	2.21	1.10	2.16	2.0e-11	
Run 1-F	90	2.03	0.463	UHR	2.24	4.7e-18	2.24	≈0.0	4.0e-5	≈0

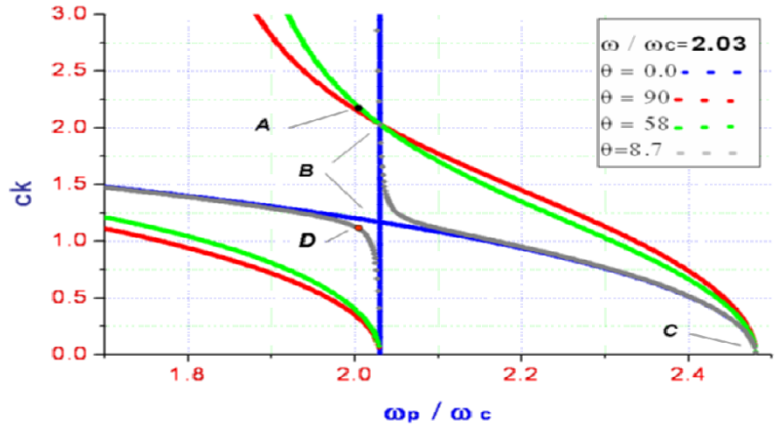

Fig. 2. Dispersion relation in the wavenumber-ω_p/ω_c space; wave frequency is $2.03\omega_c$. Blue, red, green and gray curves correspond to the wave normal angles of 0, 90, 58 and 8.7 degrees. The definitions of the points A, B, C and D are described in the text.

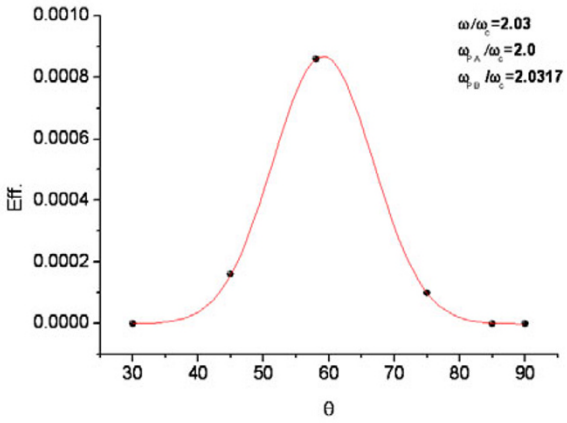

Fig. 3. The conversion efficiency as a function of the wave normal angle of the incident UHR-mode waves. The red curve is a Gaussian fitting curve.

quency is equal to the wave frequency, a part of the wave energy is converted to LO-mode waves. The other part of the wave energy is converted to Z-mode waves, which propagate further into the higher density region, while the converted LO-mode waves propagate toward the lower density region. For the calculation of the efficiency of the mode conversion process, we estimated the Poynting vector of each wave component including the incident (UHR-mode) and LO-mode waves; we calculated the ratio given by

$$\boldsymbol{E}_{\rm ff} = \boldsymbol{P}({\rm LO})/\boldsymbol{P}({\rm Inc}) \tag{13}$$

$$\boldsymbol{P} = \frac{\boldsymbol{E}_{\rm Max} \times \boldsymbol{B}_{\rm Max}}{2\mu_0} \tag{14}$$

where $\boldsymbol{E}_{\rm ff}$, $\boldsymbol{P}$, $\boldsymbol{E}_{\rm Max}$, $\boldsymbol{B}_{\rm Max}$, and μ_0 represent the efficiency, Poynting vector, maximum amplitude of the wave electric field and wave magnetic field obtained from the FFT analysis, and permeability of the vacuum, respectively. The conversion efficiency estimated from the simulation results is summarized in Table 1. In Fig. 3, we show the variation in the efficiency as a function of the wave angle. We found that the maximum conversion efficiency was obtained in Run 1-C, but the efficiency itself was very weak.

By considering Snell's law and using initial settings so that the external magnetic field vector is directed perpendicular to the density gradient, the parallel component of the refractive index should be constant during the propagation of the incident waves propagated in an inhomogeneous medium (Jones, 1987). We considered the refractive index $\boldsymbol{n} = \boldsymbol{n}_\parallel + \boldsymbol{n}_\perp$ at the conversion point where $\omega = \omega_{\rm p}$, and $\boldsymbol{n}_\parallel$ and $\boldsymbol{n}_\perp$ are parallel and perpendicular components of the refractive index, respectively, with respect to magnetic field direction. In Run 1-C, for which it is assumed that the incident wave normal angle is 58° and the wave frequency is $2.03\omega_c$, we estimated that, at the conversion point, $\boldsymbol{n}_\parallel = 0.5745$ and $\boldsymbol{n}_\perp = 0.93$ for the UHR-mode waves and that $\boldsymbol{n} = \boldsymbol{n}_\parallel = 0.5745$ for the LO-mode waves. However, for other wave normal angles, the parallel components of the refractive indexes of the UHR-mode and LO-mode waves do not become the same value, resulting in weak coupling between UHR-mode and LO-mode waves.

3.2 Case 2: double-mode conversion

We next consider the double-mode conversion process from UHR-mode wave to Z-mode and LO-mode waves and from Z-mode waves to LO-mode and UHR-mode waves. We assume incident UHR-mode waves with different wave normal angle and different wave frequencies so as to discuss the variation of the conversion efficiency.

Prior to discussing the parameter dependences, we show a typical example of the double-mode conversion process reproduced in simulation results in Fig. 4. Here we assume the same plasma parameters used in the case that $\theta = 58°$ in the previous section, except that the plasma frequency in Region-B is $\omega_{\rm pB} = 2.54\omega_c$. As discussed in the case of the single-mode conversion, a part of the incident UHR-mode waves is transmitted into Z-mode waves over the region where $\omega = \omega_{\rm pe}$ in the inhomogeneous medium while the other part of the wave energy is reflected toward the Region-A as UHR-mode and LO-mode waves through the single-mode conversion process. Under the present con-

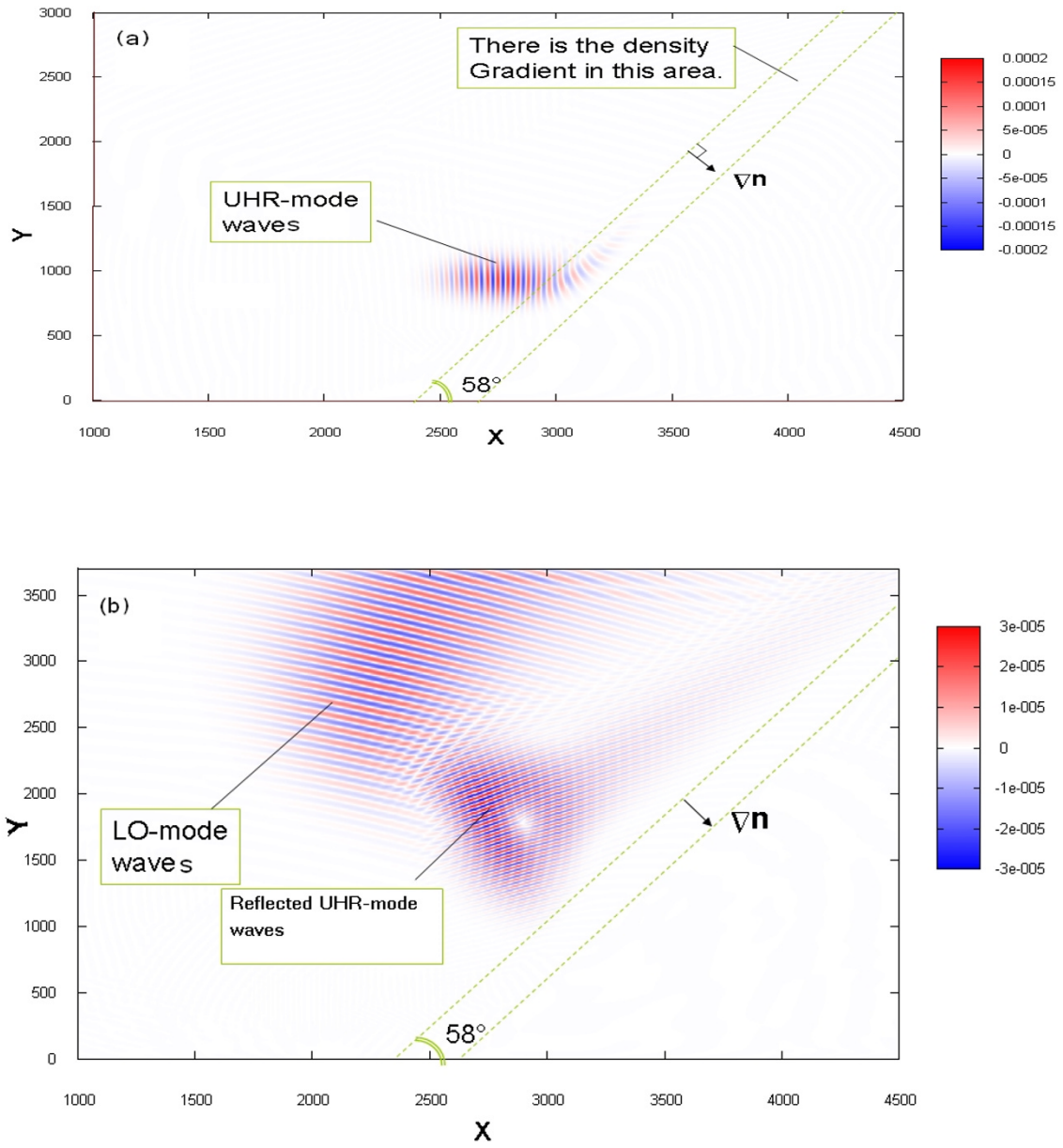

Fig. 4. Spatial distribution of the E_x component of the electric field in the simulation system at (a) $t = 52.5\omega_c^{-1}$ and at (b) $t = 157\omega_c^{-1}$.

dition, however, the transmitted waves cannot propagate further into the region-B because the wave frequency is lower than the cutoff frequency of Z-mode waves in the Region-B. Therefore, the transmitted Z-mode waves are reflected when they encounter the local cutoff frequency, eventually coming back to the condition where the wave frequency reaches $\omega = \omega_{pe}$, resulting in the mode conversion from Z-mode to LO-mode waves.

Figure 4(a) and (b) indicate the spatial distributions of the E_x component at $t = 52.5\omega_c^{-1}$ and $t = 157\omega_c^{-1}$, which is before and after the mode conversion process, respectively, which occurred around $t = 60\omega_c^{-1}$. We can clearly observe the LO-mode waves in Fig. 4(b). The wave normal vectors of the converted LO-mode wave are directed almost parallel to the external magnetic field. By analyzing the polarization of the LO-mode wave ($E_x/E_z \approx 1.73$ and $k_x \approx 0.4$, $k_y \approx 1.03$), we estimate that the wave normal angle of the converted LO-mode wave is nearly 8° apart from the ambient magnetic field. The sequence of the double-mode conversion process can also be explained by Fig. 2. The point A in the diagram indicates the position of the incident wave generated in the simulation box. In the case that the incident UHR waves propagate into the region where the local plasma frequency is equal to the wave frequency, a part of the wave energy is converted to LO-mode wave, as shown by point B in Fig. 2. The other part of the wave energy is converted to Z-mode waves propagating further into the inhomogeneous plasma, until they are reflected at point C in Fig. 2, where the wave frequency becomes equal to the local cutoff frequency of Z-mode. After the reflection, the mode conversion takes place again at the point shown by the point B, and the converted LO-mode waves propagate toward the lower density region, as indicated by point D in Fig. 2.

Table 2. Summary of simulation results and parameters used in Case 2, consist of wave normal angle, incident frequency, wave length, ratio of electric field components and efficiency. For Run 2-A to 2-E, $\omega_{pA} = 1\omega_c$ and $\omega_{pB} = 1.47\omega_c$, for Run 3-A to 3-E, $\omega_{pA} = 2\omega_c$ and $\omega_{pB} = 2.54\omega_c$, and for Run 4-A to 4-E, $\omega_{pA} = 3\omega_c$ and $\omega_{pB} = 3.72\omega_c$.

	Wave normal Angle(θ)	Frequency of wave ω/ω_c	wave length $\lambda[c\Omega^{-1}]$	wave mode	(FFT analyses) E_x/E_z	E_y/E_z	(Dispersion relation) E_x/E_z	E_y/E_z	E_Z	Efficiency
Run 2-A	35	1.05	0.811	UHR	2.24	0.23	2.23	0.23	1.5e-5	0.0025
	-8		1.333	LO	1.25	0.3	1.26	0.33	8.0e-7	
Run 2-B	40	1.05	0.839	UHR	1.88	0.175	1.89	0.175	2.0e-5	0.08
	-6		1.319	LO	1.12	0.38	1.11	0.36	2.0e-6	
Run 2-C	50	1.05	0.873	UHR	1.48	0.168	1.48	0.105	2.0e-5	0.49
	-5		1.314	LO	1.12	0.26	1.1	0.25	1.5e-5	
Run 2-D	60	1.05	0.891	UHR	1.26	0.065	1.26	0.064	4.0e-5	0.051
	-7		1.325	LO	1.24	0.136	1.23	0.134	8.0e-6	
Run 2-E	75	1.05	0.903	UHR	1.11	0.027	1.10	0.027	8.0e-5	2.0e-5
	-8		1.333	LO	1.2	0.31	1.18	0.308	3.0e-9	
Run 3-A	30	2.03	0.363	UHR	7.08	0.0199	7.07	0.198	2.0e-5	1.0e-7
	-10		0.908	LO	2.35	0.35	2.4	0.33	3.0e-10	
Run 3-B	45	2.03	0.431	UHR	3.64	0.082	3.64	0.083	2.2e-5	0.025
	-10		0.908	LO	2.2	0.91	2.2	0.93	2.3e-7	
Run 3-C	58	2.03	0.451	UHR	2.78	0.042	2.7	0.043	3.0e-5	0.53
	-8		0.879	LO	1.73	0.95	1.73	0.98	2.0e-5	
Run 3-D	75	2.03	0.461	UHR	2.34	0.015	2.34	0.016	5.0e-5	0.015
	-9		0.893	LO	1.45	1.66	1.41	1.68	2.0e-7	
Run 3-E	90	2.03	0.463	UHR	2.24	4.7e-18	2.24	-0.0	4.0e-5	-0
Run 4-A	55	3.03	0.283	UHR	4.95	0.05	4.94	0.05	2.5e-6	0.0075
	-7		0.674	LO	1.75	0.85	1.73	0.83	8.0e-8	
Run 4-B	60	3.03	0.288	UHR	4.52	0.04	4.51	0.039	5.0e-6	0.115
	-5		0.659	LO	1.40	0.55	1.42	0.54	2.5e-7	
Run 4-C	64	3.03	0.291	UHR	4.25	0.33	4.25	0.032	8.0e-6	0.62
	-4		0.653	LO	1.22	0.42	1.29	0.41	2.5e-6	
Run 4-D	70	3.03	0.295	UHR	3.96	0.024	3.97	0.023	6.0e-6	0.02
	-5		0.559	LO	1.33	0.78	1.31	0.78	3.0e-7	
Run 4-E	75	3.03	0.297	UHR	3.81	0.017	3.8	0.016	6.0e-6	3.7e-6
	-5		0.659	LO	1.25	0.85	1.2	0.89	8.0e-10	

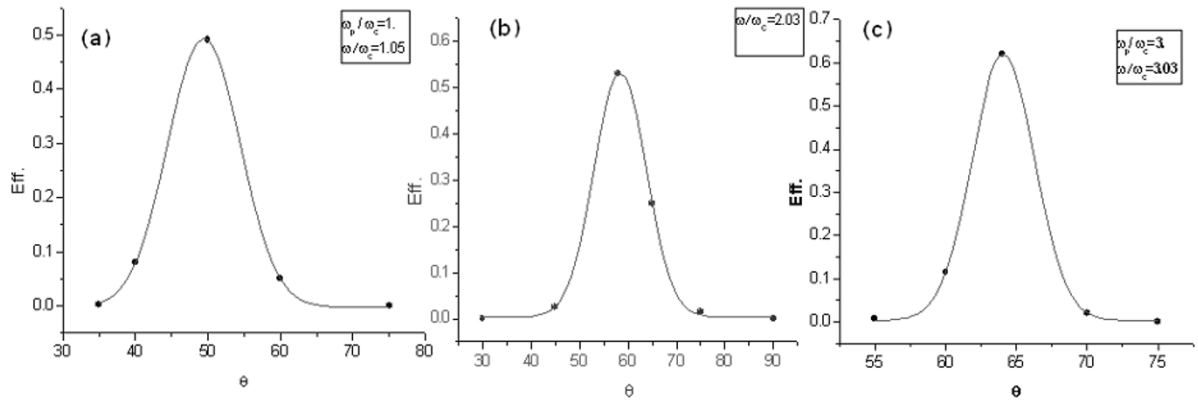

Fig. 5. Variations of the conversion efficiency depending on the wave normal angle of the incident UHR-mode waves. Each panel corresponds to the results obtained by (a) Runs 2-A to 2-E, (b) Runs 3-A to 3-E, and (c) Runs 4-A to 4-E.

3.2.1 Dependence on wave normal angle We first study the variation in the conversion efficiency with respect to its dependence on the incident wave normal angle. By assuming the same background plasma condition as used to obtain the result shown in Fig. 4, we perform five simulation runs (Run 3-A to 3-E) with different propagation angles, as given in the middle panel of Table 2, with $\omega_{pA}/\omega_c = 2$ and $\omega_{pB}/\omega_c = 2.54$. The assumed propagation angle and simulation results are summarized in Table 2, while the initial settings used in Fig. 4 correspond to Run 3-C of Table 2. Applying the same sequence used in Case 1, we analyze the simulation results in order to examine the coupling properties between UHR-mode and LO-mode waves. The obtained conversion efficiency as a function of the incident wave normal angle is shown in Fig. 5(b). We find that the highest conversion efficiency of 0.52 is obtained in Run 3-C and that the conversion efficiency decreases exponentially with varying the incident propagation angle.

3.2.2 Dependence on background plasma frequency In the previous section, we report that the high conversion efficiency was achieved in the coupling between Z-mode and LO-mode waves. Here, we study the variation in the conversion efficiency under the condition of different background plasma frequencies. As shown in upper and lower panels of Table 2, we first assume that the plasma frequency in the Region-A and Region-B to be $\omega_{pA}/\omega_c = 1$ and $\omega_{pB}/\omega_c = 1.47$, respectively, while the incident wave frequency is $\omega = 1.05\omega_c$. We also assume that $\omega_{pA}/\omega_c = 3$ and as in Region-B, $\omega_{pB}/\omega_c = 3.72$, while $\omega = 3.03\omega_c$. The efficiency for each wave normal angle estimated from simulation results is summarized in Table 2. Figure 5(a) and (c) also show the variation in the conversion efficiency as a function of the incident wave normal angle. By comparing these two parts of Fig. 5, we find that the wave normal angle corresponding to the maximum conversion efficiency changes when the background plasma frequency is varied.

Table 3. Summary of simulation results and parameters used in Case 2 (continued), consist of wave normal angle, incident frequency, wave length, ratio of electric field components and efficiency. For Run 5-A to 5-F, $\omega_{pA} = 1.\omega_c$ and $\omega_{pB} = 1.47\omega_c$, for Run 6-A to 6-E, $\omega_{pA} = 2\omega_c$ and $\omega_{pB} = 2.54\omega_c$, and for Run 7-A to 7-E, $\omega_{pA} = 3\omega_c$ and $\omega_{pB} = 3.72\omega_c$.

	Wave normal Angle(θ)	Frequency of wave ω/ω_c	wave length $\lambda[c\Omega^{-1}]$	wave mode	(FFT analyses) E_x/E_z	E_y/E_z	(Dispersion relation) E_x/E_z	E_y/E_z	E_Z	Efficiency
Run 5-A	50	0.98	1.055	UHR	1.24	4.41	1.24	4.41	1.5e-5	0.14
	=3		1.453	LO	0.39	1.11	0.37	1.10	1.5e-6	
Run 5-B	50	1.01	0.973	UHR	1.34	0.02	1.33	0.02	2.5e-5	0.40
	=6		0.475	LO	2.70	1.71	2.73	1.70	1.2e-5	
Run 5-C	50	1.05	0.873	UHR	1.48	0.10	1.48	0.10	2.0e-5	0.49
	=5		1.314	LO	1.12	0.26	1.1	0.25	1.5e-5	
Run 5-D	50	1.08	0.804	UHR	1.61	0.16	1.62	0.16	2.0e-5	0.38
	=7		1.257	LO	1.09	0.27	1.07	0.26	1.0e-5	
Run 5-E	50	1.10	0.759	UHR	1.73	0.21	1.73	0.20	2.0e-5	0.32
	=9		1.225	LO	1.13	0.28	1.10	0.26	8.0e-6	
Run 5-F	50	1.15	0.653	UHR	2.12	0.29	2.11	0.28	2.0e-5	0.12
	=11		1.142	LO	1.08	0.25	1.07	0.26	3.0e-6	
Run 6-A	58	1.95	0.583	UHR	1.88	0.074	1.88	0.074	3.0e-5	0.042
	=12		0.865	LO	0.31	1.54	0.30	1.52	5.0e-6	
Run 6-B	58	2.01	0.484	UHR	2.47	0.15	2.48	0.014	3.0e-5	0.4
	=10		1.105	LO	4.42	5.65	4.48	5.67	1.1e-5	
Run 6-C	58	2.03	0.451	UHR	2.78	0.044	2.78	0.043	3.0e-5	0.53
	=8		0.879	LO	1.73	0.95	1.73	0.98	2.0e-5	
Run 6-D	58	2.05	0.417	UHR	3.17	0.072	3.17	0.072	2.5e-5	0.46
	=9		0.846	LO	1.42	0.52	1.45	0.53	9.0e-6	
Run 6-E	58	2.08	0.364	UHR	4.0	0.11	4.05	0.11	1.0e-5	0.16
	=9		0.804	LO	1.24	0.15	1.24	0.16	3.3e-6	
Run 7-A	64	2.95	0.399	UHR	2.47	0.055	2.47	0.054	4.0e-5	0.005
	=6		0.696	LO	0.64	1.02	0.61	1.06	2.0e-7	
Run 7-B	64	3.006	0.325	UHR	3.60	0.01	3.59	0.010	1.0e-5	0.32
	=4		0.715	LO	2.6	3.4	2.8	3.7	1.9e-6	
Run 7-C	64	3.03	0.291	UHR	4.25	0.032	4.25	0.032	8.0e-6	0.62
	=4		0.653	LO	1.22	0.42	1.29	0.41	2.5e-6	
Run 7-D	64	3.06	0.245	UHR	6.0	0.066	5.90	0.064	1.1e-7	0.28
	=4		0.627	LO	1.13	0.017	1.10	0.014	2.1e-8	
Run 7-E	64	3.08	0.209	UHR	8.05	0.088	8.02	0.085	1.2e-7	0.04
	=5		0.615	LO	1.2	0.006	1.1	0.004	7.1e-9	

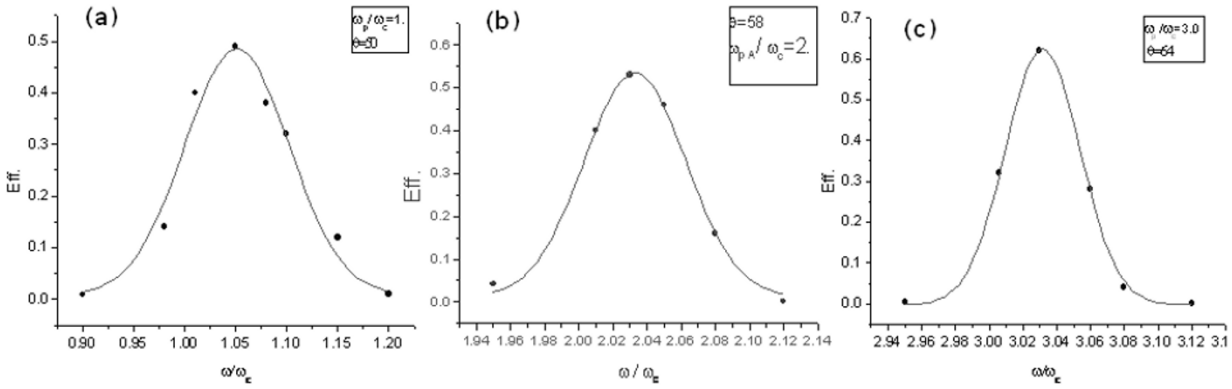

Fig. 6. Variations of the conversion efficiency depending on the wave frequency of the incident UHR-mode waves under condition of (a) $\omega_{pA}/\omega_c = 1.0$, (b) $\omega_{pA}/\omega_c = 2.0$, and (c) $\omega_{pA}/\omega_c = 3.0$.

3.2.3 Dependence on wave frequency Finally, we study the dependence of the conversion efficiency on the wave frequency of the incident UHR-mode waves. In this survey, we carry out three sets of simulations as given in Table 3, while the same ω_{pA} is assumed in each set. Namely, we assume that $\omega_{pA}/\omega_c = 1.0$, $\omega_{pB}/\omega_c = 1.47$, and $\theta = 50^\circ$ in the first set, $\omega_{pA}/\omega_c = 2.0$, $\omega_{pB}/\omega_c = 2.54$, and $\theta = 58^\circ$ in the second set, and $\omega_{pA}/\omega_c = 3.0$, $\omega_{pB}/\omega_c = 3.72$, and $\theta = 64^\circ$ in the third set. The simulation results of these sets are summarized in Table 3, and the estimated conversion efficiencies as a function of the frequency of the incident UHR-mode wave are shown in Fig. 6. The simulation results reveal that the peak of the conversion efficiency is obtained in each set of simulations and that the condition of the effective mode conversion is sensitive to the relation between the background plasma frequency and the frequency of the incident UHR-mode wave.

3.2.4 Summary and discussion of Case 2 Based on the simulation results of Case 2, we found that the conversion efficiency of the double-mode conversion process is strongly dependent on the wave normal angle and the wave frequency of the incident waves. This tendency is commonly found in simulations assuming a different plasma frequency in the simulation system. Here, we discuss the coupling properties of UHR, Z-mode, and LO-mode waves in detail based on the cold plasma theory. When we consider the dispersion relation for waves in a cold plasma,

$$\boldsymbol{n}^2 = \boldsymbol{n}_\parallel^2 + \boldsymbol{n}_\perp^2 = 1 - \frac{2X(X-1)}{2(X-1) - Y^2\sin^2\theta \pm \Gamma} \qquad (15)$$

where $\Gamma = [Y^4\sin^4\theta + 4(X-1)^2Y^2\cos^2\theta]^{1/2}$, $X = (\omega_p/\omega)^2$, $Y = \omega_c/\omega$, θ is the angle between $\boldsymbol{k}$ and $\boldsymbol{B}_0$, and the $+(-)$ sign gives the refractive index of the extraordi-

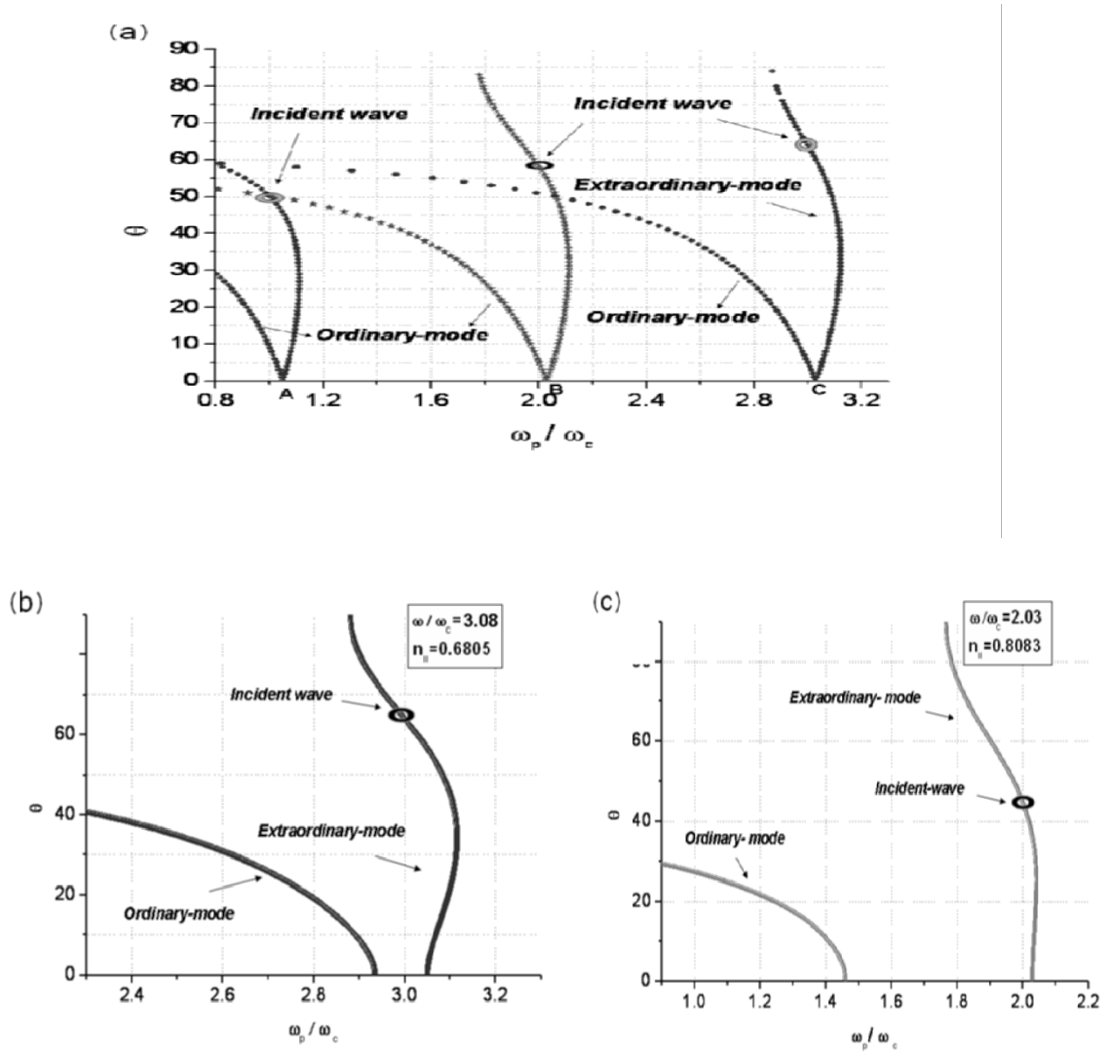

Fig. 7. (a) Variation of wave normal angle θ depending on the local plasma frequency. Red, green and blue lines correspond to the settings used in Run 2-C, 3-C, and 4-C. Under these settings, the condition in which both $\boldsymbol{n}_{\parallel} = \boldsymbol{n}_{\parallel}^{c}$ and $\boldsymbol{n}_{\perp,\mathrm{LO}} = \boldsymbol{n}_{\perp,\mathrm{Z}} = 0$ are satisfied at $\theta = 0$ as shown by the points A, B and C in the diagram, resulting in the highest conversion efficiency. (b, c) Variations of the wave normal angle θ under the cases corresponding to the condition that $\boldsymbol{n}_{\parallel} \neq \boldsymbol{n}_{\parallel}^{c}$ is satisfied at the location of the mode conversion. Each panel corresponds to the settings used in (b) Run 7-E and (c) Run 3-B.

nary (ordinary) mode. By taking Snell's law into consideration and by assuming that the external magnetic field is directed perpendicular to the density gradient, the parallel component of the refractive index should be constant during the wave propagation in an inhomogeneous medium. It is also clear from Eq. (15) that the two modes coalesce when the quantity Γ vanishes. This in turn requires that the conditions of $X = 1$ and $\theta = 0$ should be simultaneously satisfied, $\boldsymbol{n}_{\perp}^{2} = 0$. Namely, that $\boldsymbol{n}_{\perp,\mathrm{LO}} = \boldsymbol{n}_{\perp,\mathrm{Z}} = 0$ where $\boldsymbol{n}_{\perp,\mathrm{LO}}$ and $\boldsymbol{n}_{\perp,\mathrm{Z}}$ are perpendicular components of the refractive index of LO-mode and Z-mode waves, respectively. Based on this discussion, we can estimate the parallel component of the refractive index of the incident UHR-mode wave corresponding to the highest conversion efficiency in the double-mode conversion process by referring to the value of $(\boldsymbol{n}_{\parallel}^{c})^{2} = \frac{Y}{1+Y}$. Here, $\boldsymbol{n}_{\parallel}^{c}$ is a critical value for the parallel component of the refractive index obtained from Eq. (15) where the condition $\Gamma = 0$ is satisfied and two branches of ordinary mode and extraordinary mode are connected. The parallel components of the refractive index of both ordinary and extraordinary waves become the same value for the wave parameters corresponding to the highest conversion efficiency, as is expected according to Snell's law. For example, in Figs. 5(b) and 6(b), we obtain the highest conversion efficiency when we assume $\omega = 2.03\omega_{c}$ and $\theta = 58^{\circ}$. Meanwhile, the estimated critical value for the wave frequency of $\omega = 2.03\omega_{c}$ is $(\boldsymbol{n}_{\parallel}^{c})^{2} = (0.5745)^{2}$, corresponding to $\theta = 58.3^{\circ}$; these are consistent with the simulation results. Figure 7(a) shows θ determined from the dispersion relation as a function of ω_{p}/ω_{c} for the ordinary mode and extraordinary mode for the cases of $\boldsymbol{n}_{\parallel} = \boldsymbol{n}_{\parallel}^{c}$ under different settings. Figure 7(a) indicates that these two curves (extraordinary-mode and ordinary-mode branches) connect at the region where ω_{p}/ω_{c} is equal to the wave frequency under each setting. The coupling between these two modes can be strong at point A for $\theta = 50^{\circ}$, at point B for $\theta = 58.3^{\circ}$, and at point C for $\theta = 64^{\circ}$. Note that, in the case that $\boldsymbol{n}_{\parallel} \neq \boldsymbol{n}_{\parallel}^{c}$, the curves of the ordinary- and extraordinary-mode branches are disconnected for a real value of $\boldsymbol{n}_{\perp}$. This mismatch results in a decrease in the mode conversion ef-

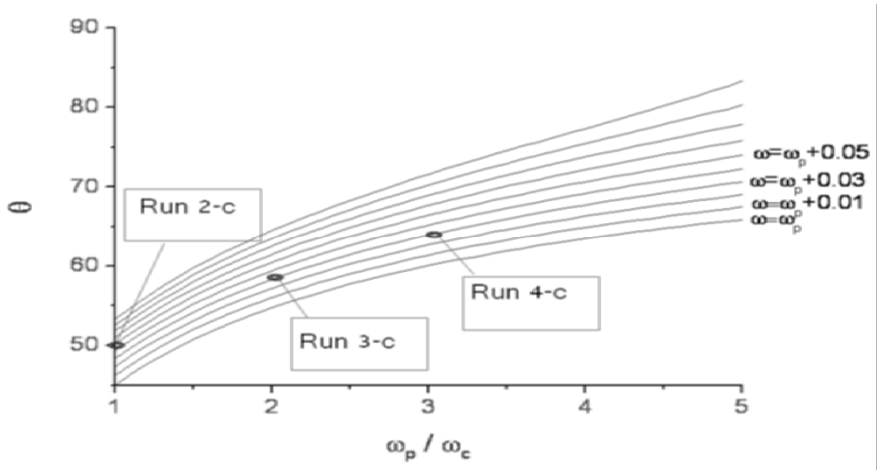

Fig. 8. Variation of the wave normal angle θ satisfying the condition of $\boldsymbol{n}_{\parallel} = \boldsymbol{n}_{\parallel}^{c}$ as a function of the local plasma frequency. Each curve shows the contour line of the wave frequency normalized by the local plasma frequency; contour lines are drawn every $0.01\omega_{\mathrm{p}}$. The rings indicate the positions of three incident wave normal angles that used in Run 2-C, 3-C, and 4-C.

ficiency. Two typical examples are shown in Fig. 7(b) and 7(c). The region of evanescence develops between the two branches, and the mode conversion can only take place by the effect of tunneling through the evanescent region. By referring to these results, we find that the estimations based on the theory are consistent with the simulation results.

Based on this exploration and on the results of the simulation, we can also estimate the incident angle corresponding to the highest efficiency. Figure 8 shows the relation among the wave frequency, incident wave normal angle, and background plasma frequency that lead to the most efficient mode conversion. The lowest curve, corresponding to $\omega \approx \omega_{\mathrm{p}}$, indicates that the smallest wave normal angle θ_{Low} increases with increasing background plasma frequency. For the highest mode conversion efficiency, the wave normal angle to the incident wave should be in the range of $\theta_{\mathrm{Low}} \leq \theta < \pi/2$.

In each set of simulations for both Cases 1 and 2, we changed the initial wave normal angles of incident UHR-mode waves having a fixed wave frequency so as to be able to discuss the dependence of conversion efficiencies. In these simulations, the spatial scale of the density gradient is fixed to five wavelengths of incident waves. This assumption is used so as to clarify the fundamental properties of the conversion process. However, since the wavelength itself varies depending on the initial wave normal angle, this assumption is equivalent to the condition that the different spatial gradient is assumed in each run. Figure 9 shows the relative spatial scale of the density gradient used in the simulations of Run 3 with different wave normal angles, while values are normalized by the scale used in Run 3-C, L_0. Under the condition that the spatial scale of the density gradient is sufficiently larger than the wavelength of the incident UHR-mode waves, as we discuss later, the effect of the variation shown in Fig. 9 would be negligible because the conversion efficiency rapidly decreases with deviations from the critical wave normal angles. However, as has been shown in Fig. 10(a), in the case that the density gradient is close to the wavelength of the waves, the conversion efficiency varies depending on the spatial scale of the density

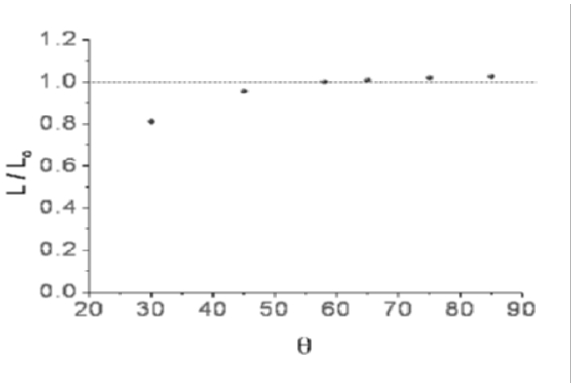

Fig. 9. The spatial scale of the inhomogeneous region used in Runs 3-A to 3-E. The values are normalized by the scale used in Run 3-C (L_0).

gradient. Even though the spatial scale of the density gradient shown in Fig. 10(a) is of the same order, the wavelength scale variation significantly alters the conversion efficiency. We should therefore pay attention to this point when we apply the results of this study to the discussion of the mode conversion process under the realistic condition.

Here, however, we would like to discuss the fundamental properties of the mode conversion process by assuming one propagation angle of incident waves and by normalizing the inhomogeneity with the wavelength of the wave. Under the condition that the incident waves have the broad-band frequency spectra, the spatial scale of the inhomogeneity seen by each wave component should become different from each other, and the resultant wave spectra of converted LO-mode waves would be influenced by the variation in the conversion efficiencies due to this difference. Our simulation model can handle such broad-band incident waves and can discuss the efficiencies of the conversion process under the condition in which waves having various wavelengths coexist. For future discussions on these simulation results under the broad-band settings, our results should serve as important clues for understanding the properties of the conversion processes.

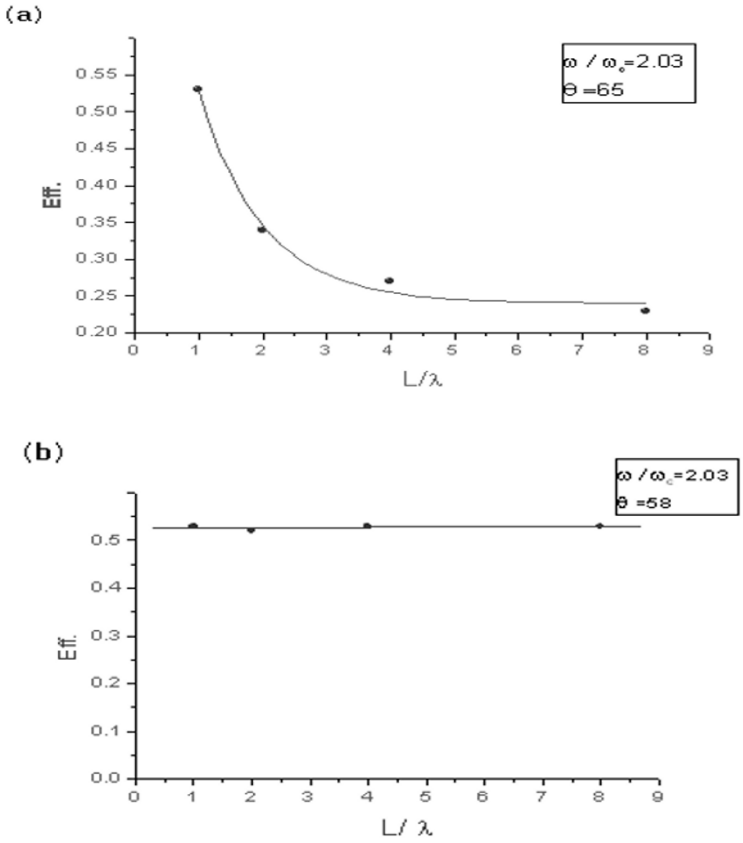

Fig. 10. Conversion efficiency as a function of the spatial scale of the density gradient in the case of (a) $\omega = 2.03\omega_c$ with $\theta = 65^\circ$ and (b) $\omega = 2.03\omega_c$ with $\theta = 58^\circ$. The former case correspond to the condition in which the curves of the extraordinary and ordinary mode branches are disconnected for the real number of $n_\perp$, while in the latter case the curves of the extraordinary and ordinary mode branches are connected for the real number of $n_\perp$.

3.3 Case 3: effects of the spatial scale of the density gradient

In the previous section, we report that the mismatch of the refractive index at the site of mode conversion results in the decrease of the conversion efficiency (Fig. 7(b) and (c)). As shown in Fig. 7, the width of the mismatch is described by the difference in local plasma frequencies between the locations where the wave normal angles of ordinary- and extra-ordinary-mode waves become zero. Under the WKB approximation, the difference in local plasma frequencies is described by the variation in the number density of the plasma medium in a spatial scale sufficiently larger than the spatial scale of wavelength. In the case that the spatial scale of the density gradient is the order of wavelength, however, we can expect efficient mode conversion due to the tunneling effect (Katoh and Iizima, 2006) even if the mismatch of the local plasma frequencies prevents the close coupling of plasma waves.

If $\boldsymbol{n}_\parallel \neq \boldsymbol{n}_\parallel^{\mathrm{c}}$, the ordinary- and extraordinary-mode branches do not meet for real values of $\boldsymbol{n}_\perp$. Therefore, the width of the mismatch that develops between these branches and mode conversion can only take place by tunneling through the evanescent zone. Since the efficiency of the tunneling effect varies depending on the spatial scale of the density gradient (Katoh and Iizima, 2006), we change the width (L) of the inhomogeneous region to λ, 2λ, 4λ, or 8λ according to the wavelength of the incident waves. Here, we note that the spatial resolution used in our study is high enough to describe the propagation of plasma waves in the simulation system properly; as an example, one wavelength of incident UHR-mode waves is expressed by using over 45 grids in the case that the local plasma frequency is $2.0\Omega_e$ and the wave frequency is $2.03\Omega_e$, with the wave normal angle of 65°.

We considered two examples typically showing the effect of the steepness of the density gradient. In the first case, we assume that $\theta = 65^\circ$ for $\omega = 2.03\omega_c$ while $\omega_{pA} = 2.0\omega_c$ and $\omega_{pB} = 2.54\omega_c$, which corresponds to the condition where $\boldsymbol{n}_\parallel \neq \boldsymbol{n}_\parallel^{\mathrm{c}}$. The results of the simulation show that the efficiency of the mode conversion increases exponentially with decreasing width of the inhomogeneous region, as shown in Fig. 10(a). In the second case, as a comparison with the first case, we assume that $\theta = 58^\circ$ for $\omega = 2.03\omega_c$, while the plasma frequencies in Region-A and Region-B are the same as those used in the first case. Note that parameters assumed in the second case correspond to the condition where $\boldsymbol{n}_\parallel = \boldsymbol{n}_\parallel^{\mathrm{c}}$. The simulation results shown in Fig. 10(b) reveal that the conversion efficiency obtained under the case of the critical wave normal angle is independent of the width of the inhomogeneous region. The simulation results shown in Fig. 10(a) and (b) suggest the possibility that, by considering the steepness of the density gradient, we can apply the mode conversion theory to explain the observational results that are inconsistent with estimations reported in previous studies. Here, we estimate the ratio δ of the grid size over L to describe the spatial scale of the inhomogeneous region.

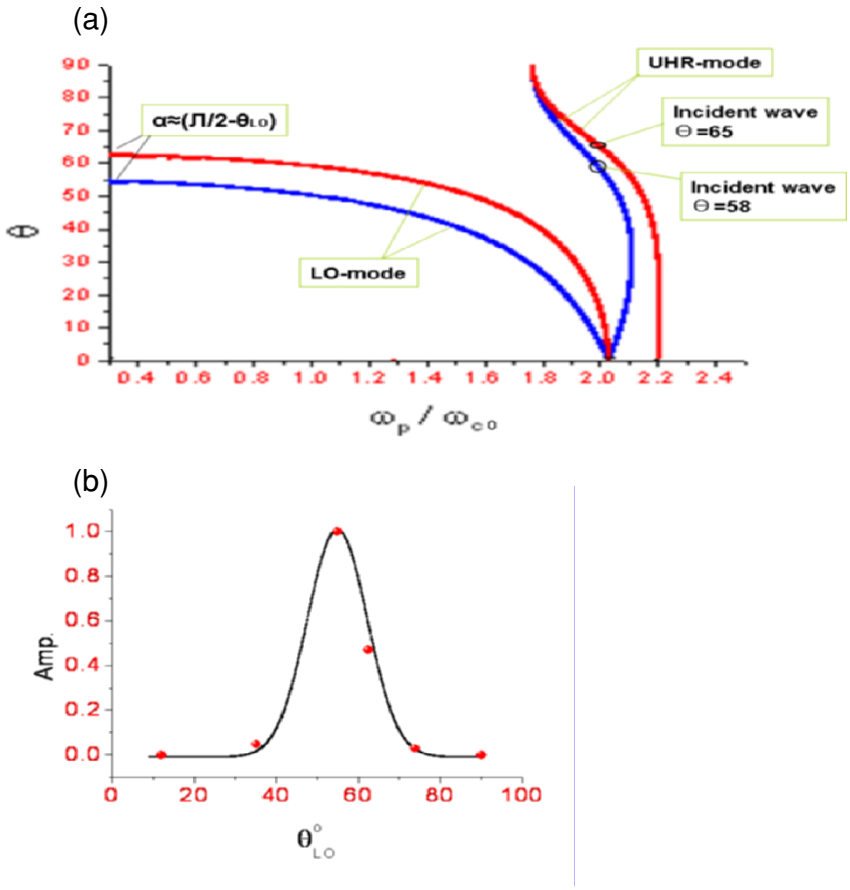

Fig. 11. (a) Variation of wave normal angle θ depending on the local plasma frequency ω_p for the case that $\omega = 2.03\omega_{c0}$ with initial incident wave normal angles of $\theta = 58^\circ$ (blue curve) and $\theta = 65^\circ$ (red curve). The beaming angle $\alpha = \pi/2 - \theta$ estimated from the asymptotic value of the blue curve is consistent with the prediction of the LMCW theory, while the estimated beaming angle from the red curve is smaller than the predicted beaming angle. (b) The relative wave amplitude profile as a function of estimated wave normal angle of LO-mode waves escaping to free space.

For the first case, assuming $\theta = 65^\circ$ for $\omega = 2.03\omega_{ce}$, δ is 1.34×10^{-2} for $L = \lambda$, 6.7×10^{-3} for $L = 2\lambda$, 3.4×10^{-3} for $L = 4\lambda$ and 1.7×10^{-3} for $L = 8\lambda$. For the second case, δ is 1.36×10^{-2} for $L = \lambda$, 6.8×10^{-3} for $L = 2\lambda$, 3.4×10^{-3} for $L = 4\lambda$, and 1.7×10^{-3} for $L = 8\lambda$.

Jones (1987, 1988) applied the linear mode conversion "window" (LMCW) theory to explain the generation process of nonthermal continuum radiation. The prediction of the LMCW theory is that the LO-mode radiation emanating from the radio window is beamed away from the magnetic equatorial plane at an angle $\alpha = \tan^{-1}\sqrt{\omega_c/\omega_p}$ (Jones, 1988), while the frequency of waves emitted from the radio window is determined by the local plasma frequency at the site of mode conversion. For the incident wave with $\omega = 2.03\omega_c$, the prediction of LMCT is $\alpha = 35^\circ$. The beaming angle can be also estimated by the asymptotic value of the wave normal angle toward the lower plasma density region. Figure 11(a) indicates the variation of the wave normal angle as a function of ω_p/ω_{c0} for $\theta = 58^\circ$ (blue curve) under the condition that $\boldsymbol{n}_\parallel$ is constant, where ω_{c0} is the local electron cyclotron frequency at the conversion point. We estimate 35° of the wave normal angle, which is consistent with the LMCT prediction. However, by considering the effect of the steep density gradient, we obtain a smaller value of the wave normal angle of LO-mode waves. As an example, we show the variation of the wave normal angle in the case of $\theta = 65^\circ$ (red curve) in Fig. 11(a). In this case, we obtain the asymptotic value of 28°, showing that the wave radio angle could be smaller than that of the LMCT prediction. This discrepancy is explained by the limitation of the LMCT theory, which assumes that the mode conversion only occurs in the case of the close coupling of plasma waves at the site of mode conversion. Jones' alpha is related to the condition that two branches of the ordinary and extraordinary mode are connected. Under such condition, obviously the wave radio angle becomes the same as the LMCT prediction. In our study, even in the case that two branches are separated, we show that the mode conversion takes place with satisfying the Snell's law in the case that the density gradient is on the order of the wavelength. Figure 11(b) shows the relative wave amplitude profile as a function of radio window angle obtained from the results of Fig. 5(b). The relative wave amplitude in each angle is estimated from the conversion efficiency by comparison with the value of Run 3-C.

Therefore, under the condition that efficient mode conversion is expected due to the effect of the steep density gradient, the radio window angle of LO-mode waves could be smaller than the LMCT prediction, as recently pointed out by Hashimoto *et al.* (2005) and Boardsen *et al.* (2008).

4. Conclusions

We report here our studies on the properties of the mode conversion processes using 2D electron fluid simulations. Our simulation results confirm that the wave energy of the UHR-mode waves tend to be converted into the LO-mode waves through the mode conversion process. As a first case, we considered the single-mode conversion process with different wave normal angle and found that the efficiency of the mode conversion from UHR-mode wave to LO-mode wave was weak and that a large amount of wave energy was converted to the transmitted Z-mode waves. We also found that the results of our study are consistent with those of previous theoretical works. In our second case, we considered the double-mode conversion process, including the mode conversion process from Z-mode to LO-mode waves, and we obtained high conversion efficiencies in this coupling process. We also performed the theoretical estimation of the conversion process by analyzing the dispersion relation of the cold plasma. We confirmed that the maximum conversion efficiency obtained in the simulation results is explained by the matching of the perpendicular component of the refractive index of waves at the site of the mode conversion. We studied the relation between the incident wave normal angles and the background plasma frequency that leads to the highest conversion efficiency.

The conversion process from Z-mode waves to LO-mode waves, discussed in Case 2, has been studied theoretically by Jones (1987), who treats mode conversion processes using the warm plasma theory with the density gradient perpendicular to the background magnetic field. Our simulation results indicate that the wave normal angle of LO-mode waves is nearly parallel to magnetic field at the site of mode conversion, which is consistent with previously reported results, such as those of Jones (1976, 1987) and Lembege and Jones (1982). We also found that there is a possibility that we can apply the mode conversion theory for the explanation of observation results that are inconsistent with estimations reported in the previous studies. The simulation results of Case 3 revealed that, by considering the steepness of the density gradient, we can expect efficient mode conversion, even in the case that the mismatch of the refractive indexes prevents the close coupling of plasma waves.

The results of our study demonstrate that our simulation model can adequately treat plasma wave processes in an inhomogeneous plasma medium. We have considered the oblique of propagation of the incident UHR waves while the density gradient is fixed to the perpendicular direction to the external magnetic field. This assumption can be applied to the equatorial region of the plasmapause in the Earth's inner magnetosphere and to the case of field-aligned irregularities in the polar region. On the other hand, although we can expect that an efficient conversion process does take place in the storm-time inner magnetosphere, the assumption used in our study may be violated under such disturbed plasma conditions. By assuming initial plasma settings inferred from the observation data, we can discuss the conversion process under a realistic condition in the disturbed plasma condition; such studies will be important in the future study.

Acknowledgments. The authors would like to express their sincere thanks to both reviewers for the constructive comments and suggestions. The computations were performed by the KDK system of research Institute for Sustainable Humanosphere (RISH) at Kyoto University as a collaborative research project. This work was supported by Tohoku University Global COE program "Global Education and Research Center for Earth and Planetary Dynamics" and by Grant-in-Aid for Scientific Research (21840011) from the Ministry of Education, Culture, Sports, Science and Technology of Japan.

References

Benson, R. F., Source mechanism for terrestrial kilometric radiation, *Geophys. Res. Lett.*, **2**, 52–55, 1975.

Boardsen, S. A., J. L. Green, and B. W. Reinisch, Comparison of kilometric continuum latitudinal radiation patterns with linear mode conversion theory, *J. Geophys. Res.*, **113**, A01219, doi:10.1029/2007JA012319, 2008.

Jones, D., Source of terrestrial non-thermal radiation, *Nature*, **260**, 686–689, 1976.

Jones, D., Mode-coupling of Z-mode waves as a source of terrestrial kilometric and Jovian decametric radiations, *Astron. Astrophys.*, **55**, 245–252, 1977.

Jones, D., Latitudinal beaming of planetary radio emissions, *Nature*, **288**, 225–229, 1980.

Jones, D., The magnetopause as a source of nonthermal continuum radiation, *Phys. Scr.*, **35**, 887–894, 1987.

Jones, D., Planetary radio emissions from low magnetic latitudes—observations and theories, in *Planetary Radio Emissions II*, edited by Rucker, H. O., S. J .Bauer, and B. M. Pedersen, 255–293, Austrian Acad. Sci., Vienna, Austria, 1988.

Hashimoto, K., R. R. Anderson, J. L. Green, and H. Matsumoto, Source and propagation characteristics of kilometric continuum observed with multiple satellites, *J. Geophys. Res.*, **110**, A09229, doi: 10.1029/2004JA010729, 2005.

Hashimoto, K., J. L. Green, R. R. Anderson, and H. Matsumoto, Review of kilometric continuum, in *Lecture Notes in Physics*, edited by J. W. LaBelle and R. A. Treumann, vol. 687, pp. 37–54, Springer, New York, 2006.

Katoh,Y., Hybrid simulations of particle acceleration processes due to wave particle interactions, Ph.D. thesis, Tohoku University, Sendai, 2003.

Katoh, Y. and M. Iizima, A computer simulation study on the mode conversion process from slow X-mode to fast X-mode by the tunneling effect, *Earth Planets Space*, e53–e56, 2006.

Kim, K. S., E. H. Kim, D. H. Lee, and K. Kim, Conversion of ordinary and extraordinary waves into upper hybrid waves in inhomogeneous plasma, *Phys. Plasma*, **12**, 052903, 2005.

Lembege, B. and D. Jones, Propagation of electrostatic upper-hybrid emission and Z mode waves at the geomagnetic equatorial plasmapause, *J. Geophys. Res.*, **87**(A8), 6187–6201, 1982.

MjΦlhus, E., Linear conversion in magnetized plasma with density gradient parallel to the magnetic field, *J. Plasma Phys.*, **30**(2), 179–192, 1983.

MjΦlhus, E., On linear conversion in a magnetized plasma, *Radio Sci.*, **25**(6), 1321–1339, 1990.

Oya, H., Conversion of electrostatic plasma waves into electromagnetic waves: numerical calculation of the dispersion relation for all wavelengths, *Radio Sci.*, **12**, 1131–1141, 1971.

Oya, H., Origin of Jovian decametric wave emissions-conversion from the electron cyclotron plasma wave to the O-mode electromagnetic wave, *Planet. Space Sci.*, **22**, 687–708, 1974.

Stix, T. H., *Waves in Plasmas*, American Institute of Physics, New York, 1992.

Takano, H., I, Nagano, and S. Yagitani, Analysis of electromagnetic wave propagation with resonance effect in collision-free magnetized plasma, *Electron. Commun. Jpn.*, **88**(10), 55–66, 2005.

Ueda, H. O., Y. Omura, and H. Matsumoto, Computer simulations for direct conversion of the Hf electromagnetic wave into the upper hybrid wave in ionospheric heating experiments, *Ann. Geophys.*, **16**, 1251–1258, 1998.

Warren, E. S. and E. L. Hagg, Observation of electrostatic resonances of the ionospheric plasma, *Nature*, **220**, 466–468, 1968.

M. J. Kalaee (e-mail: j_kalaee2000@yahoo.com), T. Ono, Y. Katoh, M. Iizima, and Y. Nishimura